Mechanism and Machine Theory 163 (2021) 104348

Contents lists available at ScienceDirect

Mechanism and Machine Theory

journal homepage: www.elsevier.com/locate/mechmachtheory

Research paper

Development of a novel leg-wheel module with fast transformation and leaping capability

Hsuan-Yu Chen[a], Ting-Hao Wang[a], Kuang-Chan Ho[a], Chuan-Yu Ko[b], Pai-Chen Lin[b], Pei-Chun Lin[a,*]

[a] Department of Mechanical Engineering, National Taiwan University, Taipei 106, Taiwan
[b] Department of Mechanical Engineering, National Chung Cheng University, Chiayi 621, Taiwan

A R T I C L E I N F O

Article history:
Received 3 November 2020
Revised 28 March 2021
Accepted 28 March 2021

Keywords:
Leg-wheel module
Leg-wheel transformation
Leaping behavior
Mechanism design
Trajectory planning

A B S T R A C T

We report on the development of a novel two-degrees-of-freedom module capable of transforming its shape between a wheel and a leg, with the length of the latter approximately 3.4 times the wheel radius. The leg-wheel module was empirically built and experimentally evaluated. It utilizes a linkage mechanism and can perform a smooth yet rapid leg-wheel transition within 0.25 s. The design concept, selection of the linkage parameters, and kinematics are described in this paper. The rapid transition from a wheel to a leg endows the robot with wheel-to-leap behavior. The general motion planning strategy of the leg-wheel, as well as the wheel-to-leap behavior, are explained in the demonstration example. The results confirm that the module can perform wheel-to-leap behavior with a height of up to 4.6 times the wheel radius.

1. Introduction

Several thousand years of man-made civilization have changed the environment, including the terrain, in many ways. In addition to natural terrain (such as mountains), the engineered landscape includes flat surfaces, surfaces with smooth curvatures, terraced fields, stairs, and single steps. While legged robots are highly capable of negotiating uneven terrain, wheeled robots are advantageous for cruising over flat terrain because of their smoothness, power efficiency, and high speed. Therefore, leg-wheel hybrid robots can effectively negotiate existing flat and rough terrains [1].

Several leg-wheel hybrid robots have been reported in the literature. They can be categorized into three types, as shown in Table 1. The robots in the first category have wheels mounted on the feet. The wheels are typically small and actively actuated. The wheels and legs are coordinated and act together to achieve locomotion. The new version of the quadruped ANYmal [2] is equipped with four non-steerable and torque-controlled wheels, achieving power-efficient motion on flat ground. The Epi.q Lizard [3] has four rotating tri-wheels as legs, which act together to perform locomotion and terrain negotiation. An exception to using the active wheel is the Roller Walker [4], which has passive wheels mounted at the end of the legs. This robot utilizes skate-like motion for locomotion. Additional examples are the TowrISIR [5], PAW [6], and Mobile Robot [7].

The robots in the second category have separate leg and wheel morphologies, which may be interchanged depending on the requirements. For example, the upper limbs of the Transleg [8], a quadruped, exhibit wheeled morphology. When the

* Corresponding author.
E-mail address: peichunlin@ntu.edu.tw (P.-C. Lin).

https://doi.org/10.1016/j.mechmachtheory.2021.104348
0094-114X/

Table 1
Characteristics of the shape-changeable leg-wheels.

Type	Robot Configuration		Actuator	Rotation	Leg Length(l)	l_{max}
Wheel		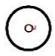	1	A	X	R
III.shape-changeable	Lingkage leg-wheel		2	A	A	3.4R
	Quattroped [20]		2	A	A	1.75
	TurboQuad [21–23]	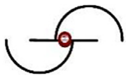	2	A	A	1.5R
	Transformable Wheels [12]		2	A	A	1.8R
	Retractable Wheel-leg Module [13]	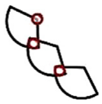	3	A	A	≥2R
	Wheel Transformer [14]		1	A	P	1.77R
	ELAN Robot [16]	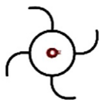	2	A	A	2.1R
	Transformable Wheel Actuated by Soft Pneumatic Actuators [17]		2	A	P	1.77R
I.	Wheels mounted on the feet [4–7]	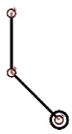	X	A/P	A	X
II.	Separate leg and wheel morphologies [8–11]	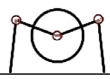	X	A/P	A	X

Note: A, P, and X indicate active-driving, passive-driving, and unknown/not available, respectively. The leg length l_{max} is represented using wheel radius as the basis.

lower limbs are retracted, the Transleg becomes a four-wheel-drive vehicle. The Chariot III [9] has two large wheels and four legs, allowing three degrees of freedom (DOFs). The Wheeleg [10] moves like a carriage, using its two front feet to pull the body, supported by a pair of wheels to advance. The RHMBot [11] contains a deformable track belt to travel on sand, gravel, and other terrains, and its tail frame supports climbing stairs.

The robots in the third category have shape-changeable leg-wheels. The wheel-track-foot transformable wheel [12] has a track on the outside of the wheel frame. When encountering obstacles, it uses the spokes inside the wheel frame to transform the entire wheel frame into feet. When swinging, the track can be used to move forward, and it can be used as a foot when standing upright. The wheel-leg retractable robot [13] can retract its limbs into a wheel for locomotion on flat ground, where the maximum leg length can be more than twice but seems less than three times the wheel radius. The Wheel Transformer [14] and Shape-morphing robot [15] are multi-terrain robots with passive transformable wheels. The legs can swing out passively for legged locomotion. The ELAN robot [16] can actively transform its wheel rim into four pieces to act as a four-spoke leg for legged locomotion. Yun et al. developed a transformable wheel mounted on soft pneumatic actuators [17]. When the actuators are activated, the expanded portion transforms the wheel into a leg. The polygonal robot [18] developed by Fei Zhang et al. is a single-legged robot consisting of multiple rods and joints. Its wheeled mode is not a perfect circle but a nine-sided polygon. Another robot with semicircular wheels [19] does not need to transform from wheel mode to legged mode; it utilizes gait changing.

Previously, we developed and reported on two generations of leg-wheel transformable robots, the Quattroped [20] and TurboQuad [21–23]. The wheels of these robots transform into C-shaped and S-shaped legs, respectively; hence, they are classified as the third category of robots. The Quattroped has a novel leg-wheel transformation module, which drives the legged motion and wheeled mode using the same actuation system. This module design and control strategy were further improved in the TurboQuad, and this robot is one of the very few robots capable of performing in situ transitions between the wheeled mode and legged gaits without stopping locomotion. However, in the current mechanism designs, the length of the robot leg is not much longer than the robot's wheel radius, so its ability to negotiate rough or uneven terrain is limited. Furthermore, the leg is not agile enough to perform dynamic behaviors, and due to the short leg length, the robot cannot perform dynamic leaping behavior.

In this paper, we report on the development of a novel leg-wheel module that not only retains the merits of our previous leg-wheel designs but also significantly increases the achievable leg length to more than 3.4 times the wheel radius. The module utilizes a multi-linkage mechanism for retraction to a wheeled shape and extension into a long leg with a point contacting the ground. Furthermore, along with the development of quadruped robots capable of dynamic motion, such as the BigDog [24], MIT Cheetah [25], and Minitaur [26], the new leg-wheel module is designed to allow rapid motion response. The leg-wheel transformation of the new module can be completed in less than a second. This characteristic further endows the possibility of developing leaping behavior because the height of the module is significantly increased when transforming the wheel into a leg. Sketches of the proposed leg-wheel module, leg-wheel mechanisms of the Quattroped and TurboQuad, and leg-wheel designs of other reported works in the third category of leg-wheel hybrid robots are listed in Table 1 for comparison. In comparison with the literature cited in the paper and summarized in Table I, the leg-wheel module described in this work has the longest leg length (i.e., 3.4R) among all the shape-changeable leg-wheels and creates the dynamic bandwidth required to perform leaping.

The remainder of this article is organized as follows. Section II describes the design of the leg-wheel in terms of the design concept, kinematics, coordinate derivation, and parameter selection. Section III reports the trajectory planning of the leg-wheel. Section IV discusses the experimental setup and evaluation. Section V concludes this paper.

2. Design of the leg-wheel module

2.1. Design concept

We are interested in developing a leg-wheel hybrid robot because its legged and wheeled modes can complementarily compensate each other in locomotion. Although many different methods can be used to hybridize the legs and wheels on the same robot platform, the series of leg-wheel transformable robots in our lab were designed to satisfy certain criteria. The first version of the robot, Quattroped [20], has the leg-wheel module design shown in Fig. 1(a). It utilizes the reconfiguration of two half-circular pieces to act as a wheel or leg. The half-circular leg is widely utilized in RHex [27] robots [28–32]. The robot has a novel leg-wheel transformation mechanism that utilizes the same set mechatronics and actuation system for both wheeled and legged motion (i.e., the hardware is hybrid), but the leg-wheel transformation requires the robot to stop its original locomotion (i.e., it is not hybrid in operation). Therefore, the redesigned robot, TurboQuad [21], has the leg-wheel module design shown in Fig. 1(b). It utilizes its own translational DOF to shift two half-circular legs to form an S-shaped leg. The robot can smoothly switch between legged and wheeled modes, as well as among different gaits in legged mode, without stopping locomotion. Furthermore, the robot uses one unified bio-inspired control strategy to handle all gait and mode generation, coordination, and transitions. Hence, the robot is hybrid not only in hardware but also in operation. With the added sensing system, the robot can automatically select the most suitable gait and mode according to the environmental conditions.

In this work, we aimed to develop a new leg-wheel module that satisfies the following criteria:

1 The robot in legged mode has body/leg morphology resembling quadrupedal mammals, with fast running and terrain negotiation capability. For example, the leg length of the antelope is slightly smaller than the distance between its two hips. Assuming the wheel radius of the robot is R, the minimum distance between its two hips (l_H) are at least $2R$. Given some clearance, here targeting $l_H = 3R$, so the maximum leg length (l_{max}) should satisfy $l_{max} \geq 3R$. The Quattroped and TurboQuad have maximum leg lengths of 1.75 R and 1.5 R, respectively. These values are not high enough to adequately exhibit the advantage of the leg, and this is one of the major reasons for developing the new leg-wheel module.
2 The dynamic response of the leg-wheel module is increased so that dramatic behavior, such as leaping, can be achieved. This criterion can be achieved using motors with strong power density, as well as by reducing the use of transmission components with large inertia. For example, the components utilized in the linear DOF of the current robots are heavy, such as a linear slider, pinion and rack, and a strong housing structure. Thus, the rotational DOF is preferred.
3 The leg-wheel has a point-contact foot. Compared to the rolling foot utilized in the Quattroped and TurboQuad, the point contact foot is easier for motion planning and can perform more delicate maneuvers on challenging terrain. Point contact is also the method utilized by quadrupedal mammals.

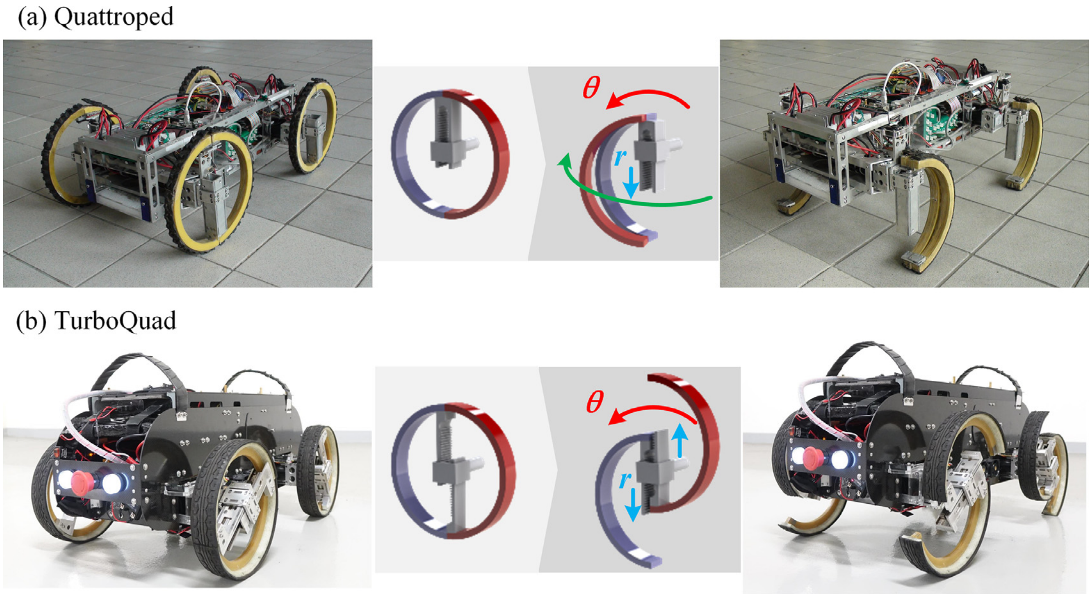

Fig. 1. Leg-wheels of the Quattroped (a) and TurboQuad (b) robots. The leg-wheels of both robots have one translational and one rotational motion DOF, which the symbols ($\boldsymbol{r}, \boldsymbol{\theta}$) represent. The green arrow in (a) indicates the extra DOF for leg-wheel transformation. The TurboQuad (b) utilizes its linear DOF for leg-wheel transformation, so no additional DOF are needed.

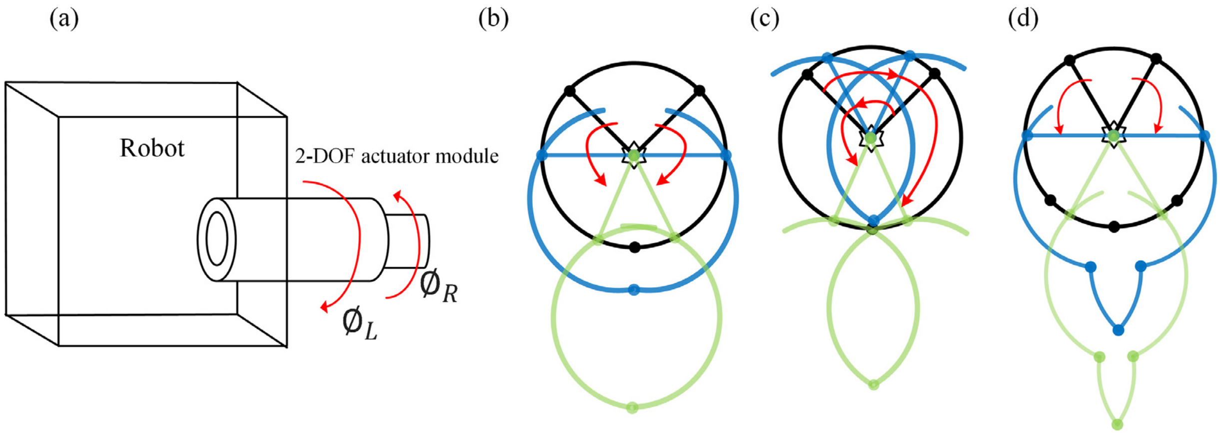

Fig. 2. Design of linkage leg-wheel mechanisms using five-bar and seven-bar linkages. (a) Schematic drawing of the 2-DOF coaxial and rotational shaft, which drives the leg-wheel; (b) leg-wheel transformation using a five-bar linkage mechanism: (b) outward and (c) inward motions; (d) leg-wheel transformation using a seven-bar linkage mechanism.

To simultaneously satisfy design criteria 1–3, a linkage mechanism with two rotational DOFs was adopted. The use of one translational DOF in the Quattroped and TurboQuad was discarded because of its limitation in extending to the required leg length, as well as its heavy weight. The linkage mechanism transformed the rotational input(s) to the prescribed output(s) with a certain design freedom. This mechanism has been used to reduce the number of actuators in both legged toys and dynamic legged robots. For example, MIT's Cheetah utilizes a four-bar linkage to transmit actuator power from the hip joint to the knee joint [25], and the Minitaur utilizes a five-bar mechanism to create planar 2-DOF leg motion [33]. Because of the symmetrical shape of the wheel and the need for the robot to move in both fore and aft directions, the symmetric linkage mechanism was adopted, and it was designed to be installed within the wheel rim.

The design underwent several versions. As shown in Fig. 2(a), the robot has a 2-DOF coaxial and rotational shaft to drive the leg-wheel module. Fig. 2(b) shows the first version, which uses a five-bar linkage. This mechanism was inspired by the Minitaur's design [26], but the arrangement of linkages was redesigned to add wheel functionality. The upper two linkages, positioned in a V shape, are input linkages driven by the motors and with one of their ends fixed to the ground (i.e., the robot's body). Hereafter, they are referred to as the motor bar. The other two linkages were designed as half-circular rims, with one end pinned to the other rim and the other end connected separately to the motor bar. When both ends of the half-circular rims are connected to each other, they form a wheel. When the leg-wheel is utilized in legged mode, in

Table 2
Alternative Leg-wheel designs.

Configuration	Characteristic	Feasibility
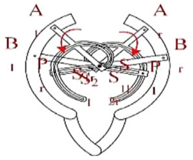	The motor bar is installed with the chute $S_{2i,i=l,r}$, which allows mounting the pin $P_{i=r,l}$ on the linkage $\overline{B_iP_i}_{\ i=r,l}$ sliding in.	1 Leg shape to be delicately designed. 2 Difficult to develop into a real mechanism due to empirical considerations, such as friction, rigidity, and fabrication methods.
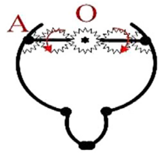	Gears are mounted directly on the motor bar to drive the gears mounted on the upper rim.	1 Noncircular gears are required if smooth leg extension and retraction motion is desired.
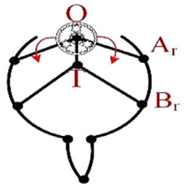	A planetary gear set is utilized to keep OT in the middle of two motor bars, and the sun gear and ring gear are fixed on the left and right motor bars, respectively.	1 This design is ideally feasible. 2 Empirically difficult to realize due to the constrained design space.
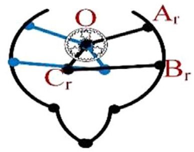	Separates their grounds into two points at different locations. A gear set is connected to the deformed R motor to adjust the angle of the motor bar $\overline{OA}$ and short linkage $\overline{OC}$.	1 The coupled motions of the R motor and θ motor make the selection of a motor difficult. 2 The gear set also requires a custom design.
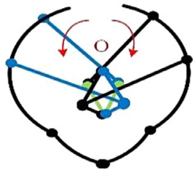	The number of linkages $N_{bar} = 15$, and the number of joints $N_{joint} = 20$. Substituting these values into Eq. (1) yields 2 DOFs.	1 The mechanism is difficult to realize due to the large number of linkages. 2 The complexity involved in optimizing linkage lengths, and the limited leg length.

which the motor bars drive the half-circular rims away from the central axis, the foot shape changes dramatically. Before the leg is fully extended, the foot exhibits a peach shape (i.e., the blue linkages in Fig. 2[b]). The shape-changing foot, as well as the discontinuous ground contact caused by the foot's peach shape, results in poor legged performance. Fig. 2(c) shows the second version. The linkage is the same as in the first version, but two DOFs move in opposite directions in the transformation, which allows for the foot's point contact. However, the linkage design effort was not trivial because the designs have a high possibility of yielding linkage collision during transformation. Furthermore, mapping between the actuator speeds and the foot speeds varies dramatically, so leg control is not easily achieved. Hence, this design was also discarded.

Fig. 2(d) shows the revision using seven-bar linkage, where each half-circular rim is cut into two pieces. The upper-two rim pieces are used for leg-length changes, while the lower-two rims form a point-contact foot. Hereafter, the upper and lower pieces of the wheel rim are referred to as the upper left/right rim and the lower left/right rim, respectively. The mechanism has $N_{bar} = 7$ linkages and $N_{joint} = 7$ joints. According to Gruebler's equation [24], the mechanism has four DOFs:

$$\mathrm{DOF} = 3\left(N_{bar} - N_{joint} - 1\right) + N_{joint} = 4 \quad (1)$$

The two additional DOFs result from free rotation between the upper and lower rims in the given motor bar configuration. In the design process, two methods were utilized to search for possible solutions to reduce the extra 2 DOFs. One is to constrain the relative motions of links (i.e., adding gears or slots), and the other is to adapt Gruebler's equation (i.e., adding links and joints). Several designs considered during the design process are shown in Table 2.

Fig. 3 shows the final design of the leg-wheel module utilized in this work; Fig. 3(a) and 3(b) illustrate the wheeled and legged modes, respectively. By adding four linkages connecting the motor bars and the upper rims, the motions of the upper rims can be precisely defined and controlled. The motions of the upper rims further define the motions of the lower left/right rims. Specifically, the motors directly drive the inner five-bar linkage, which is formed by OAE and its mirror linkages. Then, the five-bar linkage further drives the upper rims through the four-bar linkages formed by ABCD and its mirror. Finally, two four-bar linkages drive the lower rims. The mechanism has 11 linkages and 14 joints, so it has two DOFs, which satisfy criterion 2:

$$\mathrm{DOF} = 3(11 - 14 - 1) + 14 = 2 \tag{2}$$

2.2. The kinematics of the leg-wheel module

The forward/inverse kinematics of the leg-wheel module between the actuator space and the foot configuration space are required for the robot's operation. The hip joint offers two rotational and coaxial DOFs, which are driven by two motors through the mechanism, as shown in Fig. 2(a). As shown in Fig. 3(b), these two DOFs directly drive the two upper inner linkages (ϕ_R, ϕ_L). Because the leg-wheel mechanism is symmetrical, it is more convenient to express the leg-wheel configuration using coordinates (β, θ). The symbol β represents the relative orientation between the body and the symmetric line OG of the leg-wheel module, $-180 < \beta \le 180$. The symbol θ represents the angle included by the upper-right inner linkage and the symmetrical line OG. This parameter also represents the leg-wheel configuration level, so θ is denoted as the leg-wheel configuration parameter. The minimum θ, θ_0 indicates that the leg-wheel module is in wheeled mode; the maximum θ, $\theta_{l\ max}$, represents the leg in full extension, l_{max}. In this work, the clockwise direction of the angles is positive. Mapping between two coordinates is performed as follows:

$$\begin{bmatrix}\theta\\ \beta\end{bmatrix} = \frac{1}{2}\begin{bmatrix}1 & -1\\ 1 & 1\end{bmatrix}\begin{bmatrix}\phi_R\\ \phi_L\end{bmatrix} \tag{3}$$

$$\begin{bmatrix}\phi_R\\ \phi_L\end{bmatrix} = \begin{bmatrix}1 & 1\\ -1 & 1\end{bmatrix}\begin{bmatrix}\theta\\ \beta\end{bmatrix} \tag{4}$$

When the leg-wheel is operated in wheeled mode, two driving linkages (ϕ_R, ϕ_L) move at the same speed. In this case, β increases, but θ remains unchanged.

Following the defined coordinate system (β, θ), the foot configuration (i.e., point G) represented in the xy-coordinate, which originates at the hip joint O, is derived based on the trigonometric relationships of the linkages and through the sequential computations of the configurations of joints A–E of the leg-wheel mechanism. As shown in Fig. 3(b), the positions of joints A and B are as follows:

$$A = (l_1 sin\theta,\ l_1 cos\theta) \tag{5}$$

$$B = (Rsin\theta, Rcos\theta) \tag{6}$$

where R is the radius of the wheel. The lengths of the linkages are calculated as follows:

$$l_3 = \overline{BC} = 2R\sin\left(\frac{\pi}{2}n_{BC}\right) \tag{7}$$

$$l_7 = \overline{CF} = 2R\sin\left((n_{HF} - m)\pi - \theta_0\right) \tag{8}$$

where the symbols $n_{BC} = \widehat{BC}/\pi$ and $n_{HF} = \widehat{HF}/\pi$ represent the normalized arc length of the arc $\widehat{BC}$ and upper rim $\widehat{HF}$. The positions of joints E and D are calculated as follows:

$$E = \left(0, l_1 cos\theta - \sqrt{{l_1}^2 cos^2\theta - \left({l_1}^2 - (l_5 + l_6)^2\right)}\right) \tag{9}$$

$$(l_5 + l_6)^2 = {l_1}^2 + {E_y}^2 + 2l_1 E_y \cos(\pi - \theta) \tag{10}$$

$$D = \left(\frac{l_1 l_6}{l_5 + l_6} sin\theta,\ \frac{l_5}{l_5 + l_6} E_y + \frac{l_1 l_6}{l_5 + l_6} cos\theta\right) \tag{11}$$

The intermediate states were computed using the following trigonometric formula:

$$\overline{BD} = \sqrt{{l_2}^2 + {l_5}^2 - 2l_2 l_5 \cos(\pi - \theta - \angle \mathrm{OEA})} \tag{12}$$

$$\psi = \angle \mathrm{CBD} + \angle \mathrm{ABD} - \theta \tag{13}$$

the position of C is

$$C = (Rsin\theta + l_3 sin\psi,\ Rcos\theta - l_3 cos\psi) \tag{14}$$

Next, using the following intermediate states of lengths and angles:

$$\overline{AC} = \sqrt{{l_2}^2 + {l_3}^2 - 2l_2 l_3 \cos(\theta + \angle \mathrm{OEA})} \tag{15}$$

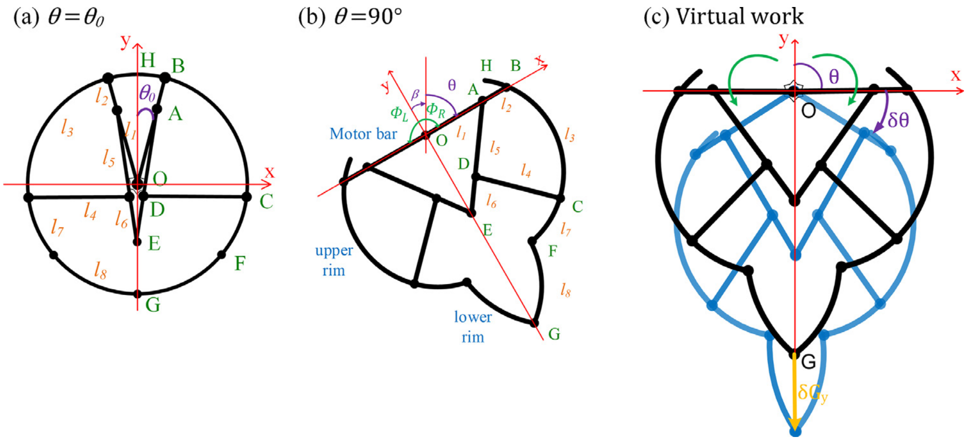

Fig. 3. The leg-wheel module in this work. (a) Configuration of the module in wheeled mode ($\theta = \theta_0$). (b) Configuration of the module in legged mode ($\theta_0 < \theta \le \theta_{l\ max}$, $\theta = 90^\circ$ in figure). (c) Notation related to the derivation of virtual work.

$$\overline{EC} = \sqrt{{l_4}^2 + {l_6}^2 - 2l_4l_6\cos(\angle\mathrm{DAC} + \angle\mathrm{DCA})} \tag{16}$$

$$\overline{EF} = \sqrt{\overline{EC}^2 + {l_7}^2 - 2\overline{EC}l_7\cos(\angle\mathrm{ECF})} \tag{17}$$

the position of F is

$$F = \left(\overline{EF}\sin\angle FEG,\ E_y - \overline{EF}\cos\angle FEG\right) \tag{18}$$

$$l_8 = \overline{FG} = 2R\sin\left((1 - n_{HF})\frac{\pi}{2}\right) \tag{19}$$

$$\overline{EG} = \overline{EF}\cos\angle\mathrm{FEG} + \sqrt{{l_8}^2 - \left(\overline{EF}\sin\angle\mathrm{FEG}\right)^2} \tag{20}$$

Finally, the position of G is calculated as follows:

$$G = G(\theta) = \left(0, E_y - \overline{EG}\right) \tag{21}$$

The position of G represents the foot configuration of the leg-wheel module, so $G(\theta)$ represents the module's forward kinematics. Eqs. (5)–(21) also reveal that although only trigonometric relationships are involved, the expanded expression of $G(\theta)$ is messy due to multi-layer substitution. Thus, the expanded expression is omitted here.

2.3. Configuration selection of the leg-wheel module

Fig. 3 reveals the rough configuration and kinematics of the proposed leg-wheel module, but the precise configuration of the module requires further investigation. The six variables need to be quantitatively defined, including θ_0, l_1, l_5, $l_5 + l_6$, n_{HF}, and n_{BC}. The remaining parameters of the leg-wheel module are passively determined by these six variables. These six variables are crucial because they determine the configuration of the leg-wheel module, including the configuration of the fully extended leg and configurations in the middle of the transformation. For example, the distance between point F and the symmetric line, F_x is negative in some variable combinations, which indicates that the linkages collide. In some variable combinations, F_x is larger than the value when the leg-wheel is in wheeled mode. This result indicates that the foot of the leg is even more obtuse than the wheel rims. Thus, we needed to impose some constraints to achieve usable results.

The selection of the leg-wheel module was executed three times, and each execution was performed based on a different goal. In the first stage of the selection, a global (or meshed) search was utilized, and the leg length (l) was set as the cost: $l > 3R$. The value F_x was constrained within a certain range, and all possible configurations of the leg wheel were checked between the wheeled form and the fully extended legged form in the specific variable set. As shown in Table 3, the search range of variables covered as many values as feasible. As shown in Table 4, the results reveal that after the selection, the largest leg length was $l_{max} \approx 445\text{mm} = 3.4R$, and 11,766 feasible combinations satisfied the requirement. The second stage included selecting combinations that do not produce inter-link collisions. This process was related to empirical realization, so some empirical considerations, such as the sizes of linkages and joints, needed to be set *a priori*. This process involved the geometrical settings of the linkages and joints, and the details are omitted here. After screening, 188 feasible combinations satisfied the requirement.

Table 3
Search range and selected parameter values of the leg-wheel module.

Variable	Search range	Selected value
θ_0 (*deg*)	$10:1:35$	17
l_1	$0.2R:0.1R:0.8R$	$0.8R$
l_5	$0.2R:0.1R:(l_5+l_6-0.2R)$	$0.9R$
l_5+l_6	$(l_1+0.2R):0.1R:(l_1+0.8R)$	$1.3R$
n_{HF}	$\frac{90}{180}:\frac{2}{180}:\frac{130}{180}$	$\frac{130}{180}$
n_{BC}	$\frac{\theta_0+10}{180}:\frac{1}{180}:\frac{180n_{HF}-\theta_0-10}{180}$	$\frac{101}{180}$

Table 4
Constraints utilized in the parameter selection of the leg-wheel module.

	Constraints	Range	Remaining solutions
1st stage	F_x (mm)	$15 \sim \mathrm{R}\sin((1-n_{HF})\pi)$	11,766
	l_{max} (mm)	> 445	
2nd stage	F_x *when* l_{max} (mm)	< 33	188
	$d_{D-\overline{OB}}$ when $d_{o-D_y} > -10$ (mm)	> 16	
	d_{O-D}	> 16	
	$d_{o-\overline{AE}}$ (mm)	> 12	
	D_x	> 4	
3rd stage	$\tau_{m\ max}$ $(\mathrm{mN}-m)$	< 4200	1
	$\frac{d\ \tau_m}{dt}$ $(\frac{\mathrm{mN}-m}{\mathrm{s}})$	< 50	

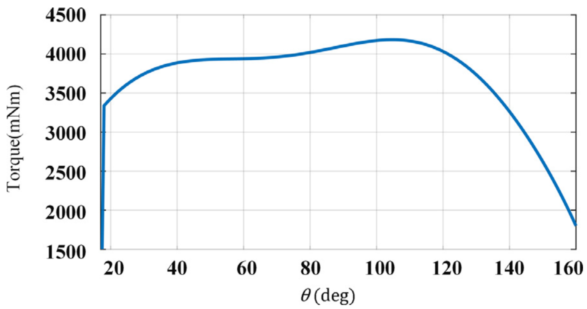

Fig. 4. Torque profile of the selected leg-wheel module using virtual work.

In the third stage of the selection, the power/torque transmission condition was utilized as the cost. The leg-wheel mechanism transmitted the actuator power at the inputs (β, θ) to the foot configuration at the output $(G_x,\ G_y)$, as shown in Fig. 3. The preferred condition was that while the input provided constant torque at a constant speed, the output similarly delivered constant force at a constant speed. Any variation in this mapping would increase the control effort. The formal analysis required use of the mechanism's dynamics. The equations of motion using the Lagrangian method were explored. However, as shown in (5)–(21), the geometric relationship between the hip joint and foot was already complicated, not to mention the derivations of these position vectors and the required matrix inverse.

The equations could not be successfully solved with any of the numerical methods we explored. Thus, a simpler method, virtual work, was utilized, where the torque required by the motor when the mechanism is in a static balance was derived. The scenario was set to be the vertical hop of the leg-wheel module ($\beta = 0$), where the input power is utilized to lift the leg-wheel module up with point contact on the ground at point G, as shown in Fig. 3(c). When the leg-wheel module was installed on the robot body, the body mass was much heavier than the leg-wheel mass. Thus, the analysis assumed that the leg-wheel module only had a point mass located at the hip (point O), and the leg-wheel mechanism itself was massless. The virtual work of the leg-wheel is as follows:

$$2\tau_m\delta\theta = mg\delta G_y \tag{22}$$

or

$$\tau_m = \frac{mg\delta G_y}{2\delta\theta} \tag{23}$$

where τ_m is the torque applied by the actuator.

The results satisfying the constraints listed in Table 4 were then inspected visually. The one with the smoothest torque profile was selected, as shown in Fig. 4. The final design of the leg-wheel module, which utilized the selected dimensions and parameters, is shown in Fig. 5(a), and the associated 2-DOF driving module is shown in Fig. 5(b).

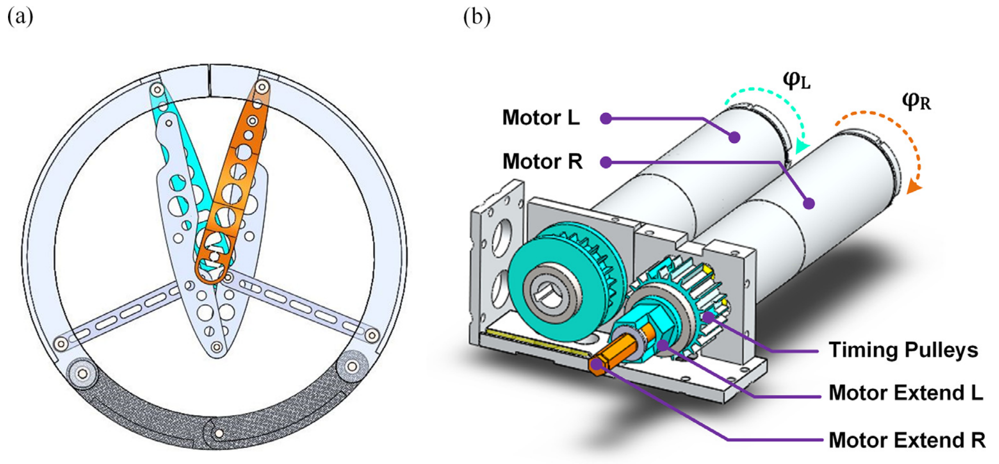

Fig. 5. The CAD drawings of (a) the leg-wheel module and (b) the 2-DOF driving module, which generates 2-DOF and coaxial rotational outputs.

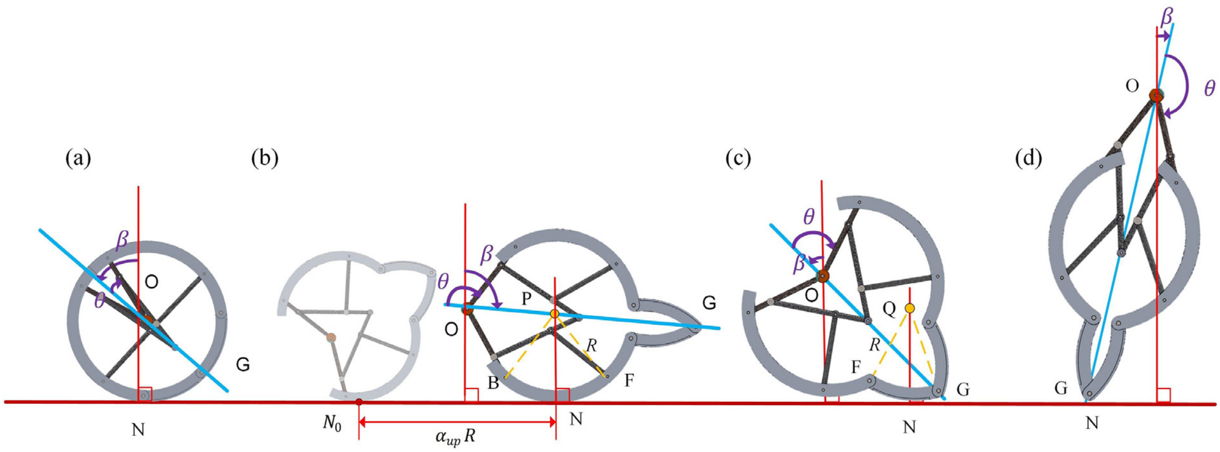

Fig. 6. The four configurations (phases) of the leg-wheel module with ground contact. (a) wheeled phase, (b) upper-rim phase, (c) lower-rim phase, and (d) foot phase.

3. Motion planning of the leg-wheel module

3.1. Phases of the leg-wheel module

The first step in motion planning involves understanding the possible configurations (phases) of the leg-wheel module. As shown in Fig. 6, they are categorized as follows:

- In the wheeled phase, where $\theta = \theta_0$ and the wheel rim contacts the ground, it does not matter which portion (the upper/lower or left/right rim) is used.
- The upper-rim phase, where $\theta \neq \theta_0$, and the upper rim contacts the ground.
- The lower-rim phase, where $\theta \neq \theta_0$, and the lower rim contacts the ground.
- The foot phase, where $\theta \neq \theta_0$, and only point G contacts the ground. This is the nominal phase when the module is operated in legged mode. In some special circumstances, the upper and lower rim phases can also be utilized for legged locomotion.
- The flight phase, wherein the leg-wheel module is in the air, and no ground contact occurs.

Following the phases definitions, as well as the forward kinematics of the leg-wheel module with respect to the hip joint O derived in Section 2.2, the forward kinematic of the leg-wheel module with respect to the inertial frame is presented here. The initial ground contact point of each phase, N_0, is set as the origin of the inertial frame. The position of the hip joint O in the inertial frame is determined by the actuation states (β, θ) versus time in this phase. Except for the flight phase, where the motion of the leg-wheel is assumed to follow ballistic flight, the other four phases have different forward kinematics and are described as follows.

In the wheeled phase, the hip-joint position O of the leg-wheel module in wheeled mode with respective to N_0 in the inertial frame can simply be expressed as:

$$O = (O_x, O_y) = (2\pi\beta, R) \tag{24}$$

In contrast, the derivation of the hip-joint position O in the other three contact phases is more complicated. In the case where the leg-wheel module rolls at its upper-rim from its initial configuration and at contact point N_0 to the instant with (β, θ), the hip-joint position O in the inertial frame can be expressed as

$$O = \vec{N_0N} + \vec{NP} + \vec{PO} \tag{25}$$

where N is the ground contact point at that instant, and point P is the center of the upper-rim. The ground contact point N can be derived as follows. The positions of points B and F, as well as P with respect to the hip joint O in the xy-coordinate, can be computed based on the kinematics described in Section 2.2. With the rotation operation of β, the xy-coordinate can be rotated to align with the principal axes of the inertial frame. At this stage, the leg-wheel is correctly oriented in the inertial frame. Next, the lowest point of the leg-wheel module is computed, and this point acts as contact point N at that instant. Thus, the angle between the initial and current contact points N_0 and N on the upper-rim can be expressed as

$$\alpha_{up} = \tan^{-1}\left(\frac{P_x - B_x}{P_y - B_y}\right) - \tan^{-1}\left(\frac{P_{x\_0} - B_{x\_0}}{P_{y\_0} - B_{y\_0}}\right) \tag{26}$$

Assuming that the leg-wheel rolls without slippage, this angel α_{up} equals the rolling angle of the upper-rim, and hence, the forward motion of the ground contact point can be computed. Thus, Eq. (25) can further be computed as

$$O = (\alpha_{up}R, 0) + (0, R) + Rot(-\beta)(-P(\theta)) \tag{27}$$

where $Rot(-\beta)$ indicates the rotation operation with angle $-\beta$.

Similarly, in the case where the leg-wheel module contacts the ground at its lower-rim, the angle between the initial and current contact points N_0 and N on the upper-rim can be expressed as

$$\alpha_{low} = \tan^{-1}\left(\frac{P_x - F_x}{P_y - F_y}\right) - \tan^{-1}\left(\frac{P_{x\_0} - F_{x\_0}}{P_{y\_0} - F_{y\_0}}\right) \tag{28}$$

The hip-joint position O in the inertial frame can then be expressed as

$$O = \vec{N_0N} + \vec{NQ} + \vec{QO} = (\alpha_{low}R, 0) + (0, R) + Rot(-\beta)(-Q(\theta)) \tag{29}$$

where Q is the center of the lower-rim.

In the case where the leg-wheel contacts the ground during its foot phase, the contact point is fixed on the ground based on the no-slippage assumption. Then, using (21), the hip-joint position O in the inertial frame can be expressed as

$$O = Rot(-\beta)(-G(\theta)) \tag{30}$$

In summary, the hip-joint position O of the leg-wheel with respect to the inertial frame defined as the initial contact point of that phase N_0 are presented in (24), (27), (29), and (30). For general leg-wheel motion, which includes several phases, the derivation of hip-joint position O requires sequential computation of the switching contact points when the phase changes.

3.2. Wheel-to-leg transition

Based on the multiple operational phases of the leg-wheel module, three methods can be utilized to transition from wheel mode to foot mode and vice versa, as shown in Fig. 7, depending on the phase in which the transition begins. The first row in Fig. 7 shows the method used when the transition begins in the upper-rim phase. The advantage of using this method is the possibility of a longer transition time, but the disadvantage is that the instant rotation center exhibits leap behavior from the contact point of the upper-rim to that of the lower rim when the lower-rim contacts the ground. Thus, the motion of the hip joint O is not smooth, as shown in Fig. 8(a), and the required motor torque is discontinuous, as shown in Fig 8(b). This phenomenon is not favored in motion planning and control. The second row represents the transition beginning in the lower-rim phase. In this case, the leg-wheel rolls on the ground, and then it switches to the point-contact phase when the leg-wheel rolls until the end of the lower rim at point G. The third row in Fig. 7 shows the method by which the transition begins in the foot phase. This method is only executable when the contact point is exactly at point G. If the leg-wheel module has forward motion, the leg extension's velocity during leg-wheel transitioning needs to be faster than the rolling speed for the contact point to be maintained at point G. Note that the leg-wheel module only uses one side of the rims in these three methods. If the leg-wheel module rolls on the other side of the rim, it needs to continuously roll until the correct side of the rim contacts the ground, and then it can leap. Furthermore, note that in empirical situations, if the original wheeled motion rolls too fast (i.e., faster than 500 mm/s), the leg-wheel module needs to decrease its forward speed for leg-wheel transition but does not need to stop.

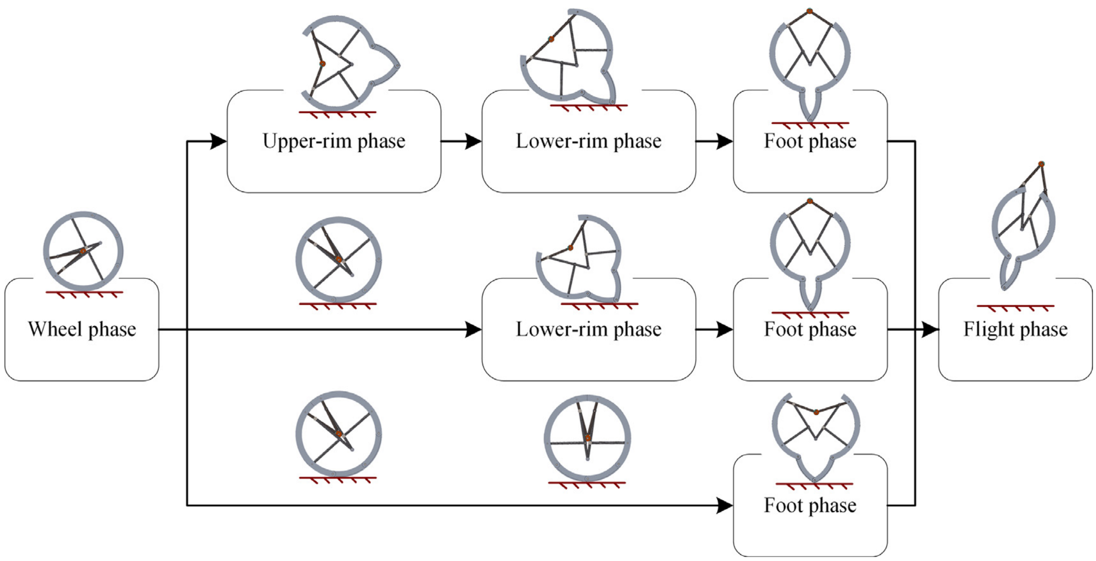

Fig. 7. The possible operating phases of the leg-wheel module and some ways the leg-wheel module can transition into a leap.

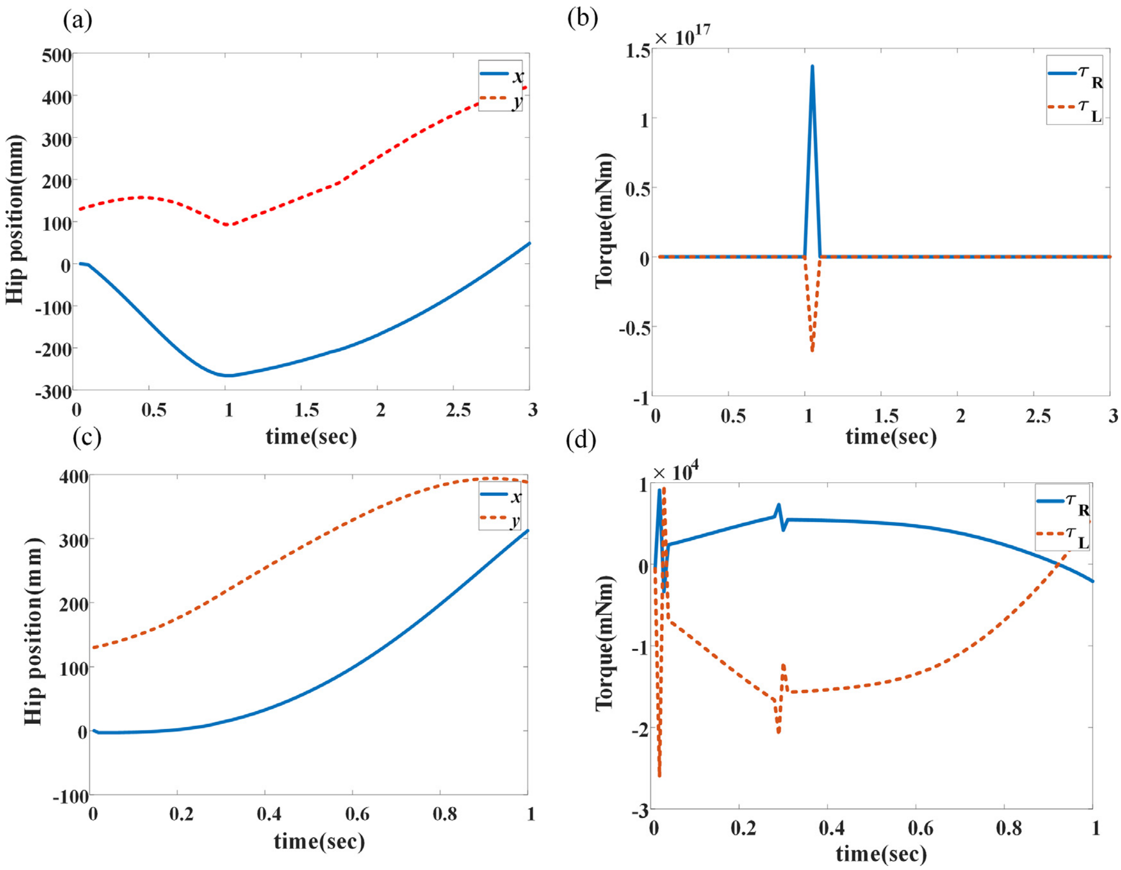

Fig. 8. Motion state of the wheel-to-leg transition, which begins in the upper-rim phase (a)(b) and the lower-rim phase (c)(d). The left column shows the horizontal (x) and vertical (y) hip-joint position O versus time, and the right column shows the required motor torque versus time.

After considering all three methods, the second method was adopted due to its smooth motion and the reasonable amount of time for leg-wheel transitioning, as shown in Fig. 8(c),(d). The leg's vertical extension and lateral forwarding are two independent DOFs, but they still need to be coordinated so that the transition can be performed in the correct phase sequence. The motion of the leg-wheel module using the second method, as well as the first method, involves mixed rolling and point-contact conditions. For a given hip-point position (point O), multiple feasible (β, θ) configurations (i.e., nonholonomic) exist, and thus, no straightforward solution exists for planning the trajectory using inverse kinematics. Therefore, the forward method should be utilized: plan (β, θ) in the joint space first, and then check the hip displacement in the Cartesian space.

3.3. Wheel-to-leap trajectory planning

In addition to ordinary operation in either the wheeled or legged mode, the unique feature of this module is its ability to perform rapid and dynamic leg-wheel transformation, allowing the robot to respond quickly to environmental changes. Because the leg length (l) is much larger than the wheel radius (R), the transformation process lifts the body up simultaneously, as shown in Fig. 7. The velocity of the leg-wheel module after transformation is dependent on how the (β, θ) states are designed during the transformation. An ordinary transformation from the wheeled mode to the legged walking or running gait requires the body to have velocity in the horizontal direction after the transformation occurs. In contrast, if upward velocity exists after the transformation, the transformation process can initiate leaping behavior. This feature is particularly useful in situations where the environment is normally flat but may include a couple of scattered obstacles. The robot can begin operating in wheeled mode, transition into legged mode to negotiate scattered obstacles (e.g., curbs along sidewalks or tree roots in the natural environment), and then transition back to wheeled mode for high-speed cruising. Therefore, this section describes the general methodology of planning the leg-wheel transformation.

The transition begins after the rolling wheel enters the lower rim (i.e., method 2). At this moment, the leg-wheel orientation is denoted as β_{TR}, and the leg-wheel configuration parameter θ starts to increase. At a certain moment, the module switches its phase from the lower rim phase to the point-contact phase. Then, the leg reaches its maximum length, $\theta_{l\ max}$, and the leg-wheel poses at the lift-off configuration, β_{LO}. Because forward leaping is preferred, the leap moment must occur in the foot-contact phase; an early leap in the lower phase usually results in a back-leap. The moment of phase transition does not need to be specified because it is passively determined by the input trajectory. The module then enters the flight phase, where the leg-wheel transforms into wheel mode to avoid a higher obstacle. The leg-wheel remains in wheel mode until touch down. In summary, the boundaries of the wheel-to-leap behavior are defined by two leg-wheel orientation configurations: β_{TR} and β_{LO}.

Several key motion moments of the leg-wheel module were quantitatively defined in the first planning step, as shown in Fig. 9. Assume that at the very beginning, the leg-wheel module is rolling on the ground continuously. The transition begins after the rolling wheel enters the lower rim (i.e., method 2). At this moment, the leg-wheel orientation is denoted as β_{TR}, and the leg-wheel configuration parameter θ starts to increase. At a certain moment, the module switches its phase from the lower rim phase to the point-contact phase. Then, the leg reaches its maximum length, $\theta_{l\ max}$, and the leg-wheel poses at the lift-off configuration, β_{LO}.

Because forward leaping is preferred, the leap moment must occur in the foot-contact phase; an early leap in the lower phase usually results in a back-leap. The moment of phase transition does not need to be specified because it is passively determined by the input trajectory. The module then enters the flight phase, where the leg-wheel transforms into wheel mode to avoid a higher obstacle. The leg-wheel remains in wheel mode until touch down. In summary, the boundaries of the wheel-to-leap behavior are defined by two leg-wheel orientation configurations: β_{TR} and β_{LO}.

The trajectories of different phases were planned separately. The planning of (β, θ) in the initial wheel phase was straightforward, where $\theta = \theta_0$, and β directly represents the wheel speed. The planning of (β, θ) in the lower rim phase was crucial for the transition. The polynomial families from linear to cubic functions and their mixtures were utilized as the nominal trajectories for evaluation. The following boundary conditions were given for the linear function: $(t_{TR}, \beta_{TR}, \theta_0)$ and $(t_{LO}, \beta_{LO}, \theta_{l\ max})$. The additional points in the middle or at one-third and two-thirds of the timeline were provided for the quadratic and cubic functions. Furthermore, two more constraints were imposed on the trajectory. First, the motion should be monotonic ($\Delta\beta \geq 0, \Delta\theta \geq 0$) to allow the leg-wheel module to move forward.

Second, the final states at t_{LO} $(\beta_{LO}, \theta_{l\ max}, \dot{\beta}_{LO}, \dot{\theta}_{l\ max})$ should result in adequate lift-off velocities for the module to proceed to the ballistic flight phase. The ideal trajectory is shown in Fig. 10. The slope of the trajectory at the starting point should be small because it directly connects to the forward wheeled motion. After the leg-wheel module takes off, it is assumed to move according to the ballistic model. Therefore, 45° is ideally the best take-off angle. Because of the same computational difficulty as in the optimization described in Section 2.3, the trajectory planning of the leg-wheel module utilized kinematic analysis. The torque of the motors in this trajectory design method may not be optimized, but the motion states of the leg-wheel can be adequately planned and controlled.

Fig. 11 shows the trajectories of the hip joint where (β_{TR}, β_{LO}) is fixed to $(-50^\circ, 10^\circ)$, and the polynomial order of (β, θ) varies with different midpoint settings. For each polynomial combination (i.e., different subplots), various trajectories with different midpoints were evaluated, and the three trajectories closest to the ideal ones were plotted. Because the trajectories in the same subplot use the same polynomial combination, the trajectories generally have similar trends.

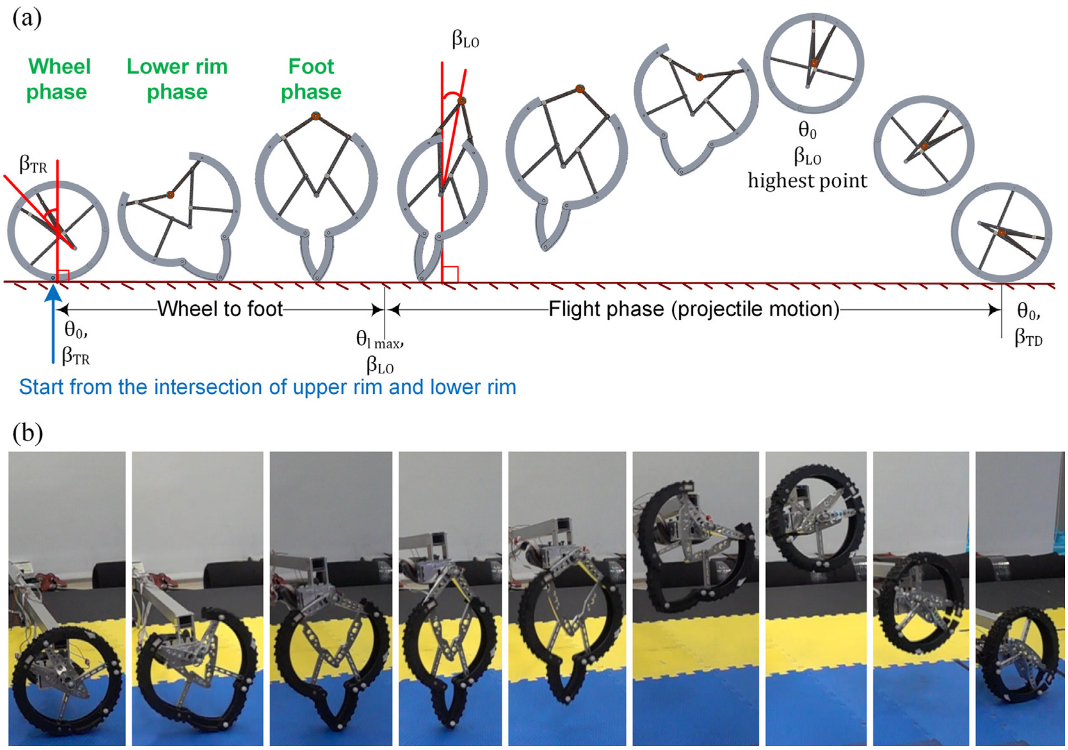

Fig. 9. Wheel-to-leap transition of the leg-wheel module: (a) illustrated configurations of the module and (b) corresponding screenshots of an experiment.

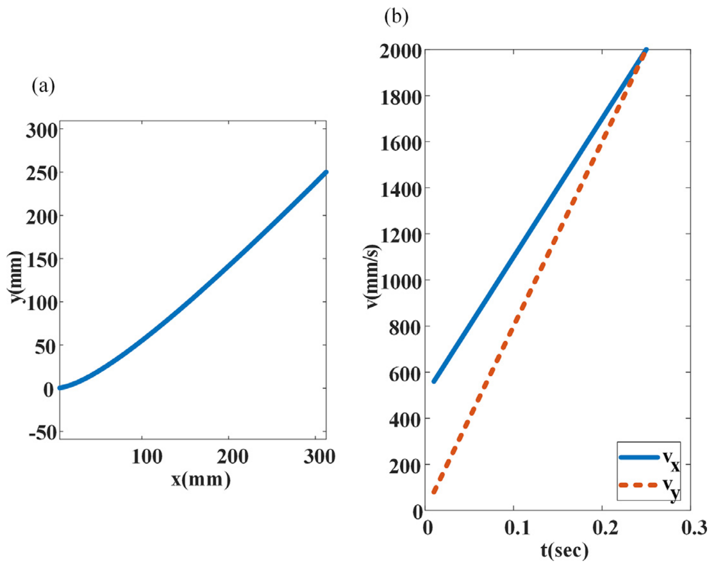

Fig. 10. The ideal leg-wheel trajectory for the module to perform wheel-to-leap behavior. (a) Planar trajectory of the hip joint in the sagittal plane. (b) Horizontal (V_x) and vertical (V_y)velocities of the hip joint versus time.

Fig. 12 shows the trajectories of the hip joint where both (β_{TR}, β_{LO}) and the polynomial order of (β, θ) varies. The selected midpoints shown in Fig. 12 are kept the same. The figure shows that many trajectories are not ideal because of their rolling back motion or horizontal take-off velocity. The remaining feasible trajectories are plotted in Fig. 13(a). Fig. 13(b) shows the displacements and velocities of the horizontal and vertical states versus time. Here, the transition time from wheel to leg is set to 0.25 s, which is the maximum speed the motor can drive the leg-wheel module. The vertical line represents the module's take-off timing. The trajectories are only plotted until the module reaches the highest point and do not include the descent.

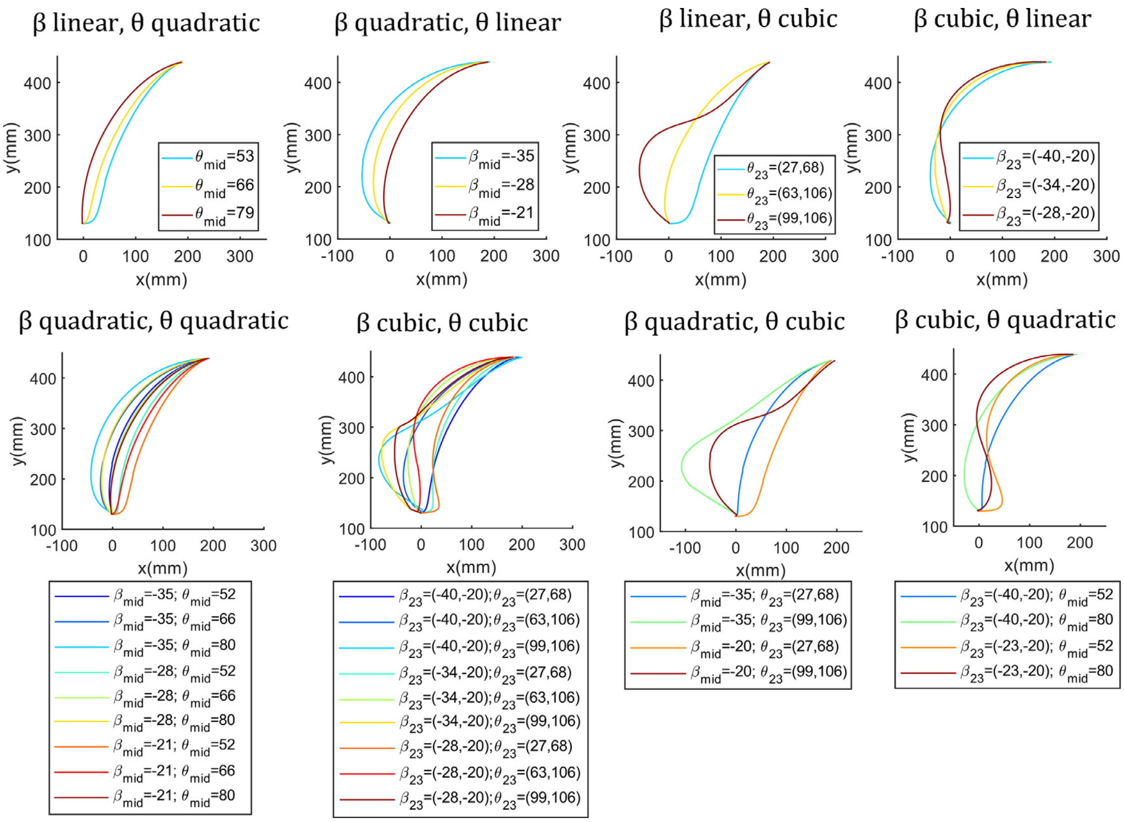

Fig. 11. Trajectories of the leg-wheel module with different polynomial settings and $(\boldsymbol{\beta_{TR}}, \boldsymbol{\beta_{LO}}) = (-50^\circ, 10^\circ)$.

After the evaluation, the parameters of the leg-wheel module's trajectory were set as $t_{LO} \in [\ 0 \quad 0.25\ ]$ s, and Eq. (31) shows the best trajectories, which utilize linear and cubic functions for (β, θ) states and have (β_{TR}, β_{Lo})= (−50°,10°) and $(\theta_0, \theta_{Lmax})$= (15°,160°) as boundary conditions. The quantitative presentation was as follows:

$$\begin{cases} \beta = 240.9639t - 50.2410 \\ \theta = 5383.3t^3 + 1056.7t^2 - 28.7394t + 17.0277 \end{cases} \tag{31}$$

After lift-off and during the flight phase, the leg-wheel module was set to transform into wheeled mode and remain in this mode until touchdown. β remained at the same speed as that of take-off, and θ transformed from $\theta_{l\ max}$ to θ_0. This leg-retracting setting allowed the module to negotiate high obstacles. The motion of the module was assumed to follow the projectile motion with lift-off velocity as the initial velocity.

4. Experiments and discussion

Fig. 14(a) shows the leg-wheel module built for experimental validation. The linkages are made of aluminum, while the joints are comprised of a steel shaft and bearing, and the wheel-rim pieces are constructed from composite materials using 3D printing technology (Mark Two Desktop 3D Printer, Markforged, Inc). The material consists of an Onyx filament (matrix), and continuous carbon fiber is used as reinforcement. The matrix material, Onyx, is printed in a triangular pattern at 37% density. The reinforcement material (continuous carbon fiber) is printed in a concentric pattern with two rings in each layer. A bicycle tire tread is mounted on the wheel rim to increase the traction force. The specifications of three generations of leg-wheel modules are listed in Table 5 for reference. The maximum leg length of the linkage leg-wheel module is much longer than its two previous versions, and the weight of the single module is also lighter than that of the TurboQuad.

The leg-wheel module is actuated using a 2-DOF driving module, as shown in Fig. 6(b), which provides two coaxial and rotational outputs. The module was modified from the driving module utilized in TurboQuad [21], which has one translational output and one rotational output. With a timing pulley, which has a transmission ratio of 1:1, motorL transmits its motion φ_L to the shaft coaxial to that of motorR. Bearings are added between the two rotational outputs, the output shaft in orange is of motor (φ_R), which is connected to the right motor bar of the leg-wheel module. The shaft in blue is of motorL through a timing pulley. Thus, the motion outputs of the motors correspond to (φ_R, φ_L), as depicted in Figs. 3(b) and 6(b). The actuators are brushless DC motors (DCX32L0028, Maxon) and are controlled by a real-time embedded control system

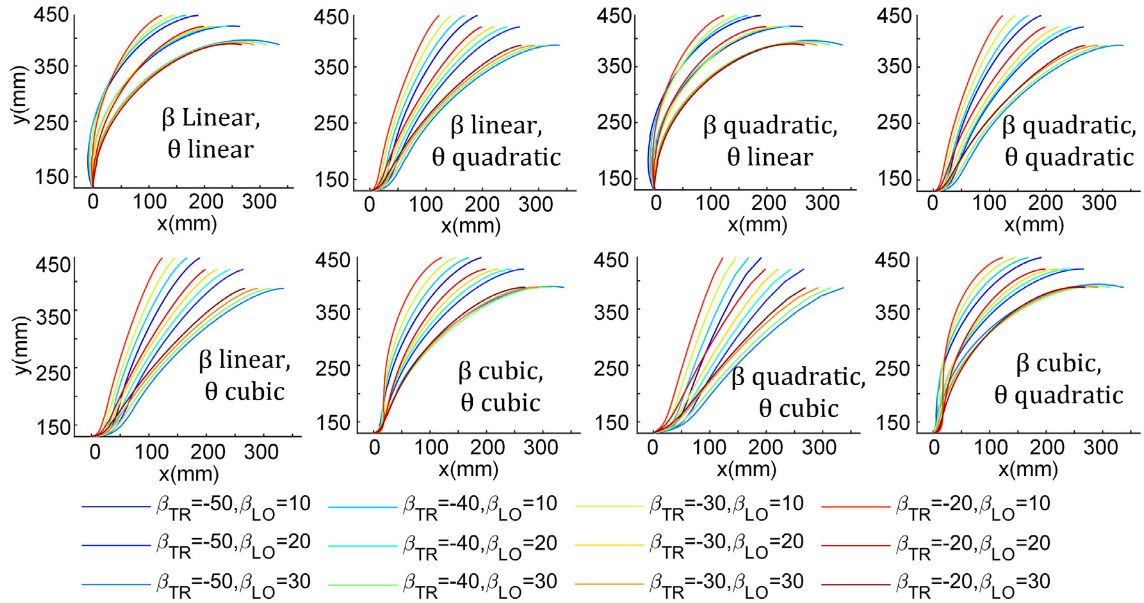

Fig. 12. Trajectories of the leg-wheel module with different polynomial settings and different (β_{TR}, β_{LO}).

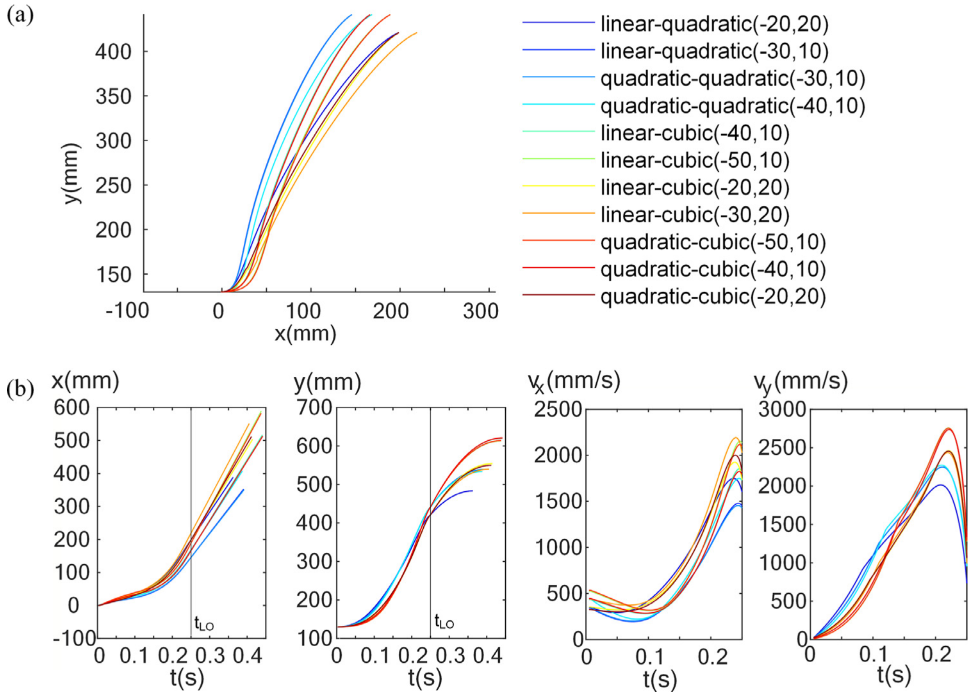

Fig. 13. Selected trajectories of the leg-wheel module that most closely fit the criteria. (a) The planar trajectory and (b) the horizontal (x) and vertical (y) components of displacement and velocity states versus time.

(myRIO, National Instruments). The main control loop runs at 1 kHz, and an integrated field-programmable gate array runs at 10 kHz.

A dry-run of the leg-wheel module was executed before conducting on-ground experiments. It was executed by the prototype version module, which did not use the second stage of screening. The θ_0 in the prototype version was 15° The leg-wheel module was fixed on the benchtop and set to track nine arbitrarily selected position commands, as listed in Table 6. The motion was intended to be very fast and simulate the required fast leg-wheel transition. The experimental results are shown in Fig. 15. Due to the fast motion, some transition points, such as point ⑥ (shown in Fig. 15[d]),

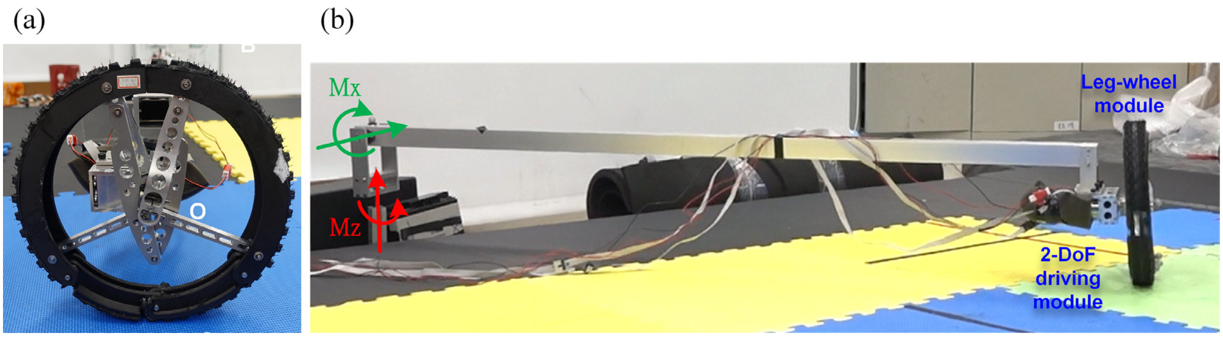

Fig. 14. The leg-wheel module: (a) side view of the module and (b) the module with a boom in experiments.

Table 5
Comparison of Quattroped, TurboQuad, and the proposed leg-wheel modules.

Robot	Quattroped	TurboQuad	Linkage leg-wheel
R (mm)	100	130	130
l_{max}(mm)	175	220	445
Mass (g)	686	1369	966
Rim material	glass fiber	3DP PC	3DP Carbon fiber

Table 6
Position commands of the leg-wheel module in dry run.

	①	②	③	④	⑤	⑥	⑦	⑧	⑨
β(deg)	−50	10	10	0	0	−30	−30	0	0
θ(deg)	15	15	160	160	75	75	160	160	15

Table 7
Specifications of the leg-wheel module in experiments.

Experiment setup	Leg-wheel module mass	2500 g
	Boom mass	1500 g
	Boom length	1 m
Planned wheel-to-leap trajectory	Transition time	0.25 s
	[Transition β, Take off β]	[-50°, 10°]
	Leap height	553.4 mm
	Leap distance	1140.5 mm
	Take-off speed Vx	2.13 m/s
	Take-off speed Vy	1.28 m/s

show a slight overshoot. The leg length in the experiment (R = 135mm, $l_{max} = 442$mm) was less than the desired length ($R = 130$mm, $l_{max} = 445$mm). We suspect that this was caused by mechanism backlash or inaccurately mounted markers of the VICON motion capture system. The markers were mounted manually based on visual observation.

In the wheel-to-leap experiments, the leg-wheel module was mounted on a 1 m boom that could rotate and swing up and down freely, as shown in Fig. 14(b). It ran on a seven-meter-long runway, and its motion was measured using a motion capture system (four high-speed T20s cameras and five high-speed V5 cameras, VICON Motion Systems). The associated parameters are listed in Table 7. The wheel-to-leap behavior of the leg-wheel module was then executed in multiple runs. Fig. 16 shows the motion states of the simplified model and the leg-wheel module in experiments from start to take-off. Table 8 lists the critical leap performance of the experimental runs, including leap height and leap distance. The wheel to

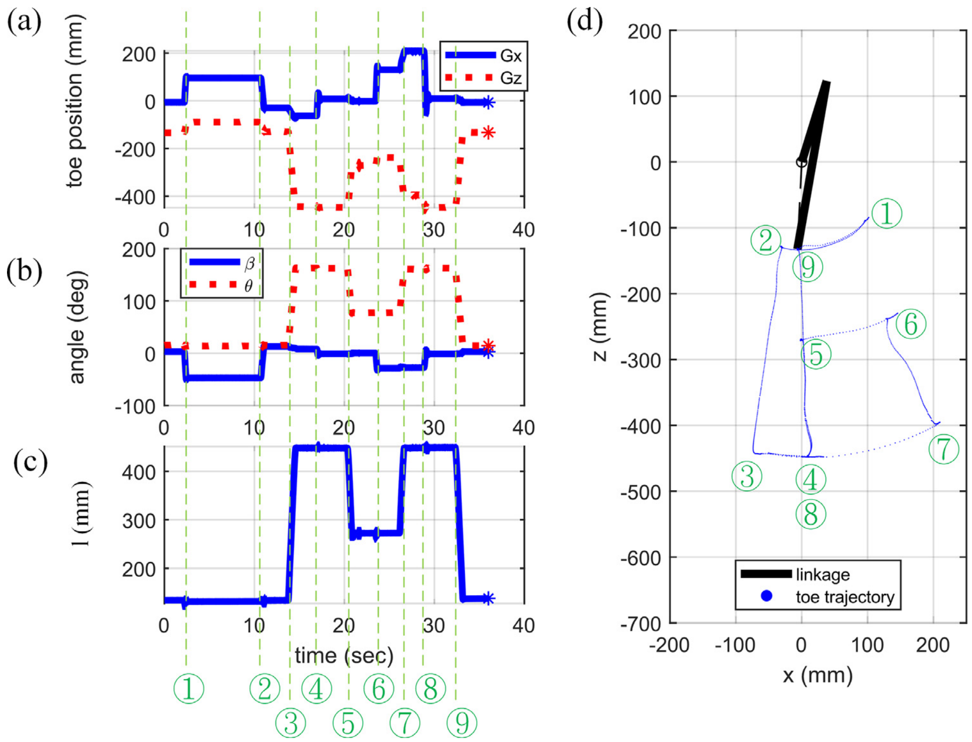

Fig. 15. The leg-wheel module in a dry-run. (a) The foot displacements, (G_x, G_y), (b) the designed (β, θ) trajectories, (c) the leg length (l), and (d) the foot trajectory.

Table 8
Performance of the leg-wheel model in wheel-to-leap motion.

Trial run	Leap height (mm)	Leap distance (mm)
1	600.6	634.1
2	610.5	487.4
3	583.9	545.0

leap behavior is a highly dynamic process. The transition only took 0.25 s, during which the leg-wheel rolled about 150 mm and then took off. The ballistic flight of the module reached a maximum average height of 598 mm, 4.6 times the wheel radius, prior to landing. The overall process took 0.75 s. While most of the motion states of the leg-wheel module matched the states estimated by the simplified model during the transition process, there was some discrepancy, especially when the module was close to take-off. We believe the discrepancy was caused by the following factors: ground slippage and the clearance and deformation of the linkage mechanism, as well as the model not accounting for the mass/inertia of the mechanism. First, the recorded encoder data of the module had the same values as the commands during the transition process (i.e., it tracked well). However, Fig. 16(a)–(c) reveals that the final leg-wheel configuration states, such as (β, θ), and leg length had lower values during take-off. This phenomenon resulted from deformation of the mechanism, and the leg-wheel had the lowest level of rigidity in this configuration. Second, the figure also reveals that the leg-wheel module took off before it was fully extended, earlier than the estimation of the simple model, which did not include the dynamics caused by the mass/inertia of the linkages and wheel rims. Only 0.01 s earlier, the module lost its final push to accelerate its speed. Third, as the leg-wheel module was taking off, the ground reaction force was decreasing to zero. This caused insufficient friction forces for the foot of the module to stay at the same ground contact point. The ground slippage resulted in non-trivial loss of forward speed, so the forward speed of the module was less than that of the simplified model, which can clearly be seen in the slopes of the curves in Fig. 16(d). In contrast, though the partially extended leg-wheel possibly resulted in the motion profile with less vertical height, the leg-wheel oriented more vertically during take-off, resulting in a higher flight height than estimated by the simplified model. Thus, there were some differences between the ballistic trajectories of the leg-wheel model and the model's estimation. Both the simulations and experiments could be improved to reduce the discrepancy between them. For example, the rigid-body dynamic model with a friction model could be utilized to take more empirical accounts into consideration. This is a complex problem for closed-chain linkages. As for the leg-wheel module, the mechanism could be optimized for less weight, clearance, backlash, and compliance. However, the efforts are non-trivial, and the improvement methods are under investigation and set aside as future work.

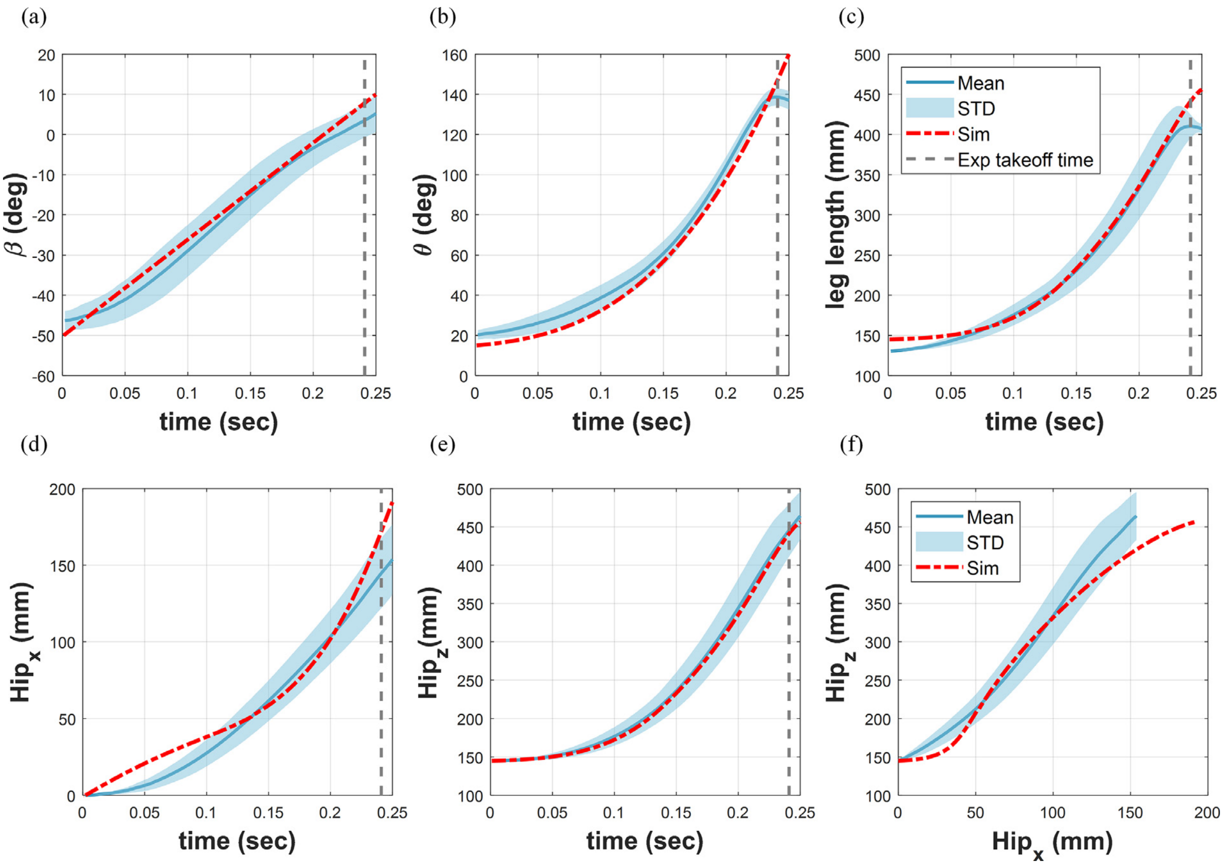

Fig. 16. The states and trajectories of the leg-wheel module while performing wheel-to-leap behavior, from start to take-off. Fig. (a)–(c) show the $(\boldsymbol{\beta}, \boldsymbol{\theta})$ states and leg length versus time. Fig. (d)–(e) show the horizontal (x) and vertical (z) hip trajectories versus time, respectively. Subfigure (f) shows the planar motion trajectory of the hip. The red dashed-dot curves represent the motion of the simplified model, and the blue curves and light blue areas are the mean and standard deviations of the module in experiments, respectively. The maximum time tick of 0.25 s is the time to take off, estimated by the model. The gray dashed lines indicate the averaged time of the module to take off in experiments, 0.01 s earlier than the time estimated by the model.

Although discrepancies exist between the simulation result and the current experimental platform, the experimental results confirm that the leg-wheel module can indeed perform significant and rapid shape transitions between the legged and wheeled morphology. This rapid transition also enables wheel-to-leap behavior, a highly dynamic transition behavior that takes less than 0.25 s, and leaps to heights of up to 4.6 times the wheel radius.

5. Conclusion

We report on the development of a novel 2-DOF leg-wheel module capable of significant shape transformation and rapid speed transition. After the concept design process and design morphology iterations, the leg-wheel module was constructed using a multi-linkage mechanism, in which the outer mechanism (i.e., wheel rim) and inner mechanism were composed of four and seven linkages, respectively. The detailed linkage configuration of the leg-wheel module was screened using a three-stage process. The first stage used leg length as the criteria, the second stage discarded the candidates that did not meet the mechanism constraints, and the third stage evaluated the power and torque transmission of the candidate mechanisms using virtual work analysis. The leg length of the final leg-wheel design is 3.4 times longer than the wheel radius. The leg-wheel module allows five types of configurations (phases) in operation: the wheel phase, upper rim phase, lower rim phase, foot phase, and flight phase. Thus, motion planning involves smooth transitioning among these phases. The planning was executed in the joint space, and the behaviors of the leg-wheel in the Cartesian space were utilized for evaluation. As the fast transition from the wheel to the long leg endows the leg-wheel with wheel-to-leap behavior, this behavior was utilized to demonstrate the motion planning process. The leg-wheel module was empirically built and experimentally evaluated. The results show that the module could achieve agile transitions between leg and wheel formation within 0.25 s and successfully triggered wheel-to-leap behavior with a height of up to 4.6 times the wheel radius, which outperformed the previous versions.

We are currently in the process of refining the design of the leg-wheel module, as well as developing a new leg-wheel transformable robot that equips this module. In the meantime, due to the fast dynamics and the potential for the robot to dramatically change between the legged mode and the wheeled mode, the new multi-leg coordination strategy is investigated.

Declaration of Competing Interest

The authors declare that they have no known competing financial interests or personal relationships that could have appeared to influence the work reported in this paper.

Acknowledgments

This work is supported by Ministry of Science and Technology (MoST), Taiwan, under contract: MOST 107–2634-F-002–004-, MOST 108–2634-F-002–002-, and MOST 109–2634-F-002–039-

Supplementary materials

Supplementary material associated with this article can be found, in the online version, at doi:10.1016/j.mechmachtheory.2021.104348.

References

[1] M. Russo, M. Ceccarelli, "A survey on mechanical solutions for hybrid mobile robots,", Robotics 9 (2) (2020) 32.
[2] M. Bjelonic, P.K. Sankar, C.D. Bellicoso, H. Vallery, M. Hutter, "Rolling in the deep–hybrid locomotion for wheeled-legged robots using online trajectory optimization,", IEEE Robot. Autom. Lett. 5 (2) (2020) 3626–3633.
[3] L. Bruzzone, G. Quaglia, R. Razzoli, "Epi. q Lizard: a modular ground mobile robot,", Proc. AIMETA (2013).
[4] G. Endo, S. Hirose, "Study on roller-walker - energy efficiency of roller-walk,", in: IEEE International Conference on Robotics and Automation (ICRA), 2011, pp. 5050–5055.
[5] W. Du, M. Fnadi, F. Benamar, Rolling based locomotion on rough terrain for a wheeled quadruped using centroidal dynamics,", Mech. Mach. Theory 153 (2020) 103984.
[6] J.A. Smith, I. Sharf, M. Trentini, "PAW: a hybrid wheeled-leg robot,", in: IEEE International Conference on Robotics and Automation (ICRA), 2006, pp. 4043–4048.
[7] H. Jiang, G. Xu, W. Zeng, F. Gao, "Design and kinematic modeling of a passively-actively transformable mobile robot,", Mech. Mach. Theory 142 (2019) 103591.
[8] Z. Wei, G. Song, G. Qiao, Y. Zhang, H. Sun, Design and implementation of a leg–wheel robot: transleg,", J. Mech. Robot. 9 (5) (2017) 051001.
[9] S. Nakajima, E. Nakano, T. Takahashi, "Motion control technique for practical use of a leg-wheel robot on unknown outdoor rough terrains,", in: IEEE/RSJ International Conference on Intelligent Robots and Systems (IROS), 2, 2004, pp. 1353–1358.
[10] S. Guccione, G. Muscato, "The Wheeleg robot,", IEEE Robot Autom. Mag. 10 (4) (2003) 33–43.
[11] Z. Luo, J. Shang, G. Wei, L. Ren, A reconfigurable hybrid wheel-track mobile robot based on Watt II six-bar linkage,", Mech. Mach. Theory 128 (2018) 16–32.
[12] F. Zhou, H. Xu, X. Zhang, "A wheel-track-leg hybrid locomotion mechanism based on transformable rims,", in: IEEE International Conference on Advanced Intelligent Mechatronics (AIM, 2017, pp. 315–320.
[13] K. Tadakuma, et al., "Mechanical design of the wheel-leg hybrid mobile robot to realize a large wheel diameter,", in: IEEE/RSJ International Conference on Intelligent Robots and Systems (IROS), 2010, pp. 3358–3365.
[14] Y.S. Kim, G.P. Jung, H. Kim, K.J. Cho, C.N. Chu, "Wheel transformer: a wheel-leg hybrid robot with passive transformable wheels,", in: IEEE Transactions on Robotics (T-RO), 30, 2014, pp. 1487–1498.
[15] S. Ryu, Y. Lee, T. Seo, "Shape-morphing wheel design and analysis for step climbing in high speed locomotion,", IEEE Robot Autom. Lett. 5 (2) (2020) 1977–1982.
[16] R. Rafique, "Reconfigurable mechanism for mobile robotic platform,", in: 1st International and 16th National Conference on Machines and Mechanisms (iNaCoMM2013), IIT Roorkee , India, 2013, pp. 714–721.
[17] S.S. Yun, J.Y. Lee, G.P. Jung, K.J. Cho, "Development of a transformable wheel actuated by soft pneumatic actuators,", Int. J. Controlz Autom. Syst. 15 (1) (2017) 36–44.
[18] F. Zhang, Y. Yu, Q. Wang, X. Zeng, H. Niu, "A terrain-adaptive robot prototype designed for bumpy-surface exploration,", Mech. Mach. Theory 141 (2019) 213–225.
[19] K. Yamamoto, T. Aoki, Development of novel mobile robot with semicircular wheels,", ROBOMECH J. 7 (1) (2020) 1–11.
[20] S.C. Chen, K.J. Huang, W.H. Chen, S.Y. Shen, C.H. Li, P.C. Lin, "Quattroped: a leg-wheel transformable robot,", IEEE/ASME Trans. Mechatron. (TMech) 19 (2) (2014) 730–742.
[21] W.H. Chen, H.S. Lin, Y.M. Lin, P.C. Lin, "TurboQuad: a novel leg–wheel transformable robot with smooth and fast behavioral transitions,", IEEE Trans. Robot (T-RO) 33 (5) (2017) 1025–1040.
[22] Y.M. Lin, H.S. Lin, P.C. Lin, "SLIP-model-based dynamic gait generation in a leg-wheel transformable robot with force control,", IEEE Robot Autom. Lett. 2 (2) (2017) 804–810.
[23] H.S. Lin, Y.M. Lin, P.C. Lin, "SLIP-model-based dynamic motion transition between different fixed points in one stride in a leg-wheel transformable robot,", in: IEEE/RSJ International Conference on Intelligent Robots and Systems (IROS), 2018, pp. 2715–2720.
[24] M. Raibert, K. Blankespoor, G. Nelson, R. Playter, "Bigdog, the rough-terrain quadruped robot,", Int. Federat. Autom. Control (IFAC) 41 (2) (2008) 10822–10825.
[25] G. Bledt, M.J. Powell, B. Katz, J.D. Carlo, P.M. Wensing, S. Kim, "MIT cheetah 3: design and control of a robust, dynamic quadruped robot,", in: IEEE/RSJ International Conference on Intelligent Robots and Systems (IROS), 2018, pp. 2245–2252.
[26] D. Blackman, J. Nicholson, C. Ordonez, B. Miller, J. Clark, Gait Development On Minitaur, a Direct Drive Quadrupedal Robot, SPIE, Unmanned Systems Technology, 2016.
[27] U. Saranli, M. Buehler, D. Koditschek, "RHex: a simple and highly mobile hexapod robot,", Int. J. Rob. Res. 20 (7) (2001) 616–631.
[28] K. Galloway, J. Clark, D. Koditschek, Variable stiffness legs for robust, efficient, and stable dynamic running,", J. Mech. Robot. 5 (1) (2013) 011009.
[29] A.M. Johnson, D.E. Koditschek, "Toward a vocabulary of legged leaping,", in: IEEE International Conference on Robotics and Automation (ICRA), 2013, pp. 2553–2560.

[30] K.J. Huang, C.K. Huang, P.C. Lin, A Simple running model with rolling contact and its role as a template for dynamic locomotion on a hexapod robot,", Bioinspir. Biomim. 9 (2014) 046004.
[31] Y.C. Chou, K.J. Huang, W.S. Yu, P.C. Lin, "Model-based development of leaping in a Hexapod robot,", IEEE Trans. Robot (T-RO) 31 (1) (2015) 40–54.
[32] W.C. Lu, M.Y. Yu, P.C. Lin, "Clock-torqued rolling SLIP model and its application to variable-speed running in a hexapod robot,", IEEE Trans. Robotics (T-RO) 34 (6) (2018) 1643–1650.
[33] G. Kenneally, D.E. Koditschek, "Leg design for energy management in an electromechanical robot,", in: IEEE/RSJ International Conference on Intelligent Robots and Systems (IROS), 2015, pp. 5712–5718.